The measurement of stress and phase fraction distributions in pre and post-transition Zircaloy oxides using nano-beam synchrotron X-ray diffraction

Document Version
Accepted author manuscript

[Link to publication record in Manchester Research Explorer](#)

The Measurement of Stress and Phase Fraction Distributions in Pre and Post-transition Zircaloy Oxides using Nano-Beam Synchrotron X-ray Diffraction

H. Swan[a] (helen.swan@nnl.co.uk), M. S. Blackmur[a] (matthew.s.blackmur@nnl.co.uk), J. M. Hyde[a] (jonathan.m.hyde@nnl.co.uk), A. Laferrere (alice.laferrere@atkinsglobal.com), S. R. Ortner[a] (susan.r.ortner@nnl.co.uk), P. D. Styman[a] (paul.d.styman@nnl.co.uk), C. Staines[b] (cassie.staines@nnl.co.uk), M. Gass[c] (mhairi.gass@amecfw.com), H. Hulme[c] (helen.hulme@amecfw.com), A. Cole-Baker[d] (aidan.cole-baker@rolls-royce.com), P. Frankel[e] (philipp.frankel@manchester.ac.uk).

[a] National Nuclear Laboratory, Building D5, Culham Science Centre, Abingdon, Oxfordshire, OX14 3DB, UK.
[b] National Nuclear Laboratory, 102B, Stonehouse Park, Stonehouse, Gloucestershire, GL10 3UT, UK.
[c] Amec Foster Wheeler Clean Energy Europe, Walton House, Birchwood, WA3 6GA, UK.
[d] Rolls-Royce plc, PO Box 2000, Derby, DE21 7XX, UK.
[e] Materials Performance Centre, School of Materials, The University of Manchester, Manchester M13 9PL, UK.

Corresponding author: Dr. Jonathan Hyde (jonathan.m.hyde@nnl.co.uk)

ABSTRACT

Zircaloy-4 oxide stress profiles and tetragonal:monoclinic oxide phase fraction distributions were studied using nano-beam transmission X-ray diffraction. Continuous stress relief and phase transformation during the first cycle of oxide growth was observed. The in-plane monoclinic stress was shown to relax strongly up to each transition, whereas in-plane tetragonal stress-relief (near the metal-oxide interface) was only observed post transition. The research demonstrates that plasticity in the metal and the development of a band of in-plane cracking both relax the monoclinic in-plane stress.

The observations are consistent with a model of transition in which in-plane cracking becomes interlinked prior to transition. These cracks, combined with the development of cracks with a through-thickness component (driven primarily by plasticity in the metal) and/or a porous network of fine cracks (associated with phase transformation), form a percolation path through the oxide layer. The oxidising species can then percolate from the oxide surface to the metal/oxide interface, at which stage transition then ensues.

1. Introduction

Zirconium alloys are used for cladding in a number of light water reactors because of their low neutron absorption cross-section, high temperature strength and relatively low susceptibility to corrosion. However, the exposure of Zircaloys to a pressurised water environment at high temperatures (~350°C) does lead to oxidation and associated hydrogen pick-up, both of which have implications for the fuel efficiency and safety, particularly at high burn-ups or extended service life.

Zircaloys oxidise in a periodic manner: the initially rapid oxide growth rate slows down to a low steady rate during the first oxidation cycle. After some time, 'transition' is reached, whereupon the oxide growth rate once again becomes rapid, then decelerates until the next transition [1,2,3]. After several of these cycles, the alloy oxidises continuously at a more rapid linear rate [4].

A mechanistic understanding of the macroscopic, microscopic and molecular-level processes (and their inter-relation) occurring during the corrosion process is key to the development of modern Zirconium-based alloys for cladding material. The evolution of the crystal structure of zirconia (in particular, the tetragonal: monoclinic phase fraction) is one molecular-level process thought to be of importance in determining the onset of transition

1

[5,6]. The tetragonal phase is known to be stabilised by high compressive stresses [7,8], as well as small grain sizes [9,10,11], therefore monitoring the progression of both monoclinic and tetragonal oxide stress profiles through transition is also of prime importance in understanding the nature of transition.

Several papers detail the use of classical X-ray diffraction (XRD) and synchrotron X-ray diffraction (SXRD) techniques to gain a fundamental understanding of the crystal structure of the oxide and associated stresses [5,12,13,14,15,16]. However, in many of these papers, the stresses and tetragonal:monoclinic phase fractions are measured with no depth resolution, but are averaged over the whole oxide layer. Trends in the average stresses or phase fractions are instead related to the sample's oxide thickness or exposure time. Techniques such as grazing incidence X-ray diffraction (GIXRD) [17] or polychromatic energy-dispersive synchrotron XRD [5] have been used to measure the stress or phase fraction profile with depth, by varying the incidence angle (in the case of GIXRD) or by making use of the whole range of X-ray beam energy (in the case of polychromatic XRD). However, these techniques, whilst giving some indication of the trends in stress and phase fraction with depth, are still averaging techniques in which the measurements are strongly weighted to the specimen surface. As such, they can only be applied with confidence to very thin oxides (sub 1-2 microns); any non-monotonic changes in the parameters of interest that may occur around transition will not be readily apparent.

Within the literature, several interpretations exist for the driving force behind the onset of accelerated oxidation (known as transition). These range from the accumulation of stresses giving rise to cracks in the oxide [12], the formation of defects such as micro-cracks and interlinking nano-pores [18,19], changes in the conductivity of the oxide layer [4], and transformation from the tetragonal to the monoclinic phase. This phase transformation has been associated with increasingly compressive stresses in the monoclinic phase at the point of transition [5], with cracking in the oxide [2], and with the linking-up of nano-porosity [15] thereby aiding the transport of the environment to the metal-oxide interface [1,15,20,21]. Pêcheur et al. [22] associated the accelerated corrosion rate to the gradual transformation of the tetragonal phase to the monoclinic phase in the protective 'barrier layer'.

None of these descriptions of transition fully explain the cause of transition, or the inter-relation between the observed oxide morphology, the stress profiles and phase fraction distributions. In this work, the in-plane and through-plane strains have been measured and the stresses calculated accordingly, for both the monoclinic and tetragonal oxide phases, fully resolved with oxide depth, for Zircaloy-4 oxide samples spanning the first three cycles of oxide growth. The tetragonal:monoclinic phase fractions have also been calculated, again fully resolved with depth. It is only by monitoring changes in stress and phase fraction distributions (and their inter-relation), *both* with oxide depth *and* for samples at different stages of oxidation, that it is possible to build up a picture of the sequence of events occurring through the corrosion process which ultimately lead to transition.

2. Experimental

2.1. Sample Preparation

Recrystallisation-annealed Zircaloy-4 tiles were mechanically polished and then pickled in a solution containing hydrofluoric acid in accordance with ASTM G2. The tiles were then exposed in 350°C water in an autoclave that was continuously refreshed with a controlled chemistry with elevated pH commensurate with typical PWR conditions. The flow rate was 15 ml·min^{-1} and a hydrogen overpressure of 1.20 bar gauge pressure was applied.

Weight gain and Scanning Electron Microscopy (SEM) measurements were performed in order to provide both overall average and local oxide thicknesses. The samples selected for examination via nano-beam synchrotron XRD are listed in Table 1 together with their oxide thicknesses derived by weight gain, oxide thicknesses as calculated from the resulting XRD data, and details of experiments performed.

Figure 1 shows where these selected samples lie on the average oxide thickness versus oxidation time curve. These oxide thicknesses are derived from weight gain measurements using the established relationship approximating 15 mg·dm^{-2} of oxygen weight gain to 1 μm of oxide growth [23]. The averages are derived from a batch of 28 samples for the early measurements. Fewer samples are involved for later measurements as specimens were removed for analysis and not returned to the autoclave. The standard deviation for the average weight gain was less than 1%, over the range of thicknesses considered. For the individual samples considered in this study, the quoted thicknesses are specimen specific, and derived from the average of three weight measurements, each separated by a balance tare operation. The largest variation in weight gain measurement in a single sample corresponded to no more than 0.03 μm.

The three thinnest samples (0.46, 1.13 and 2.09 μm oxide thicknesses) clearly lie within the first oxidation cycle. The location of the next sample (2.25 μm oxide thickness) requires some judgement. Its weight is sufficiently larger than that of the two previous average values that it may appear to be beyond the first transition. However, it should be noted that the average measurements preceding this data point show a decrease in oxide thickness. This apparent loss of weight is not related to spalling, and its cause is unclear. If a trend line (power or logarithmic) is fitted to the average oxide thicknesses for the first cycle, the sample with 2.25 μm oxide thickness appears to be late in the first oxidation cycle. Either way, it should be noted that the onset of transition cannot be instantaneous across a whole sample; near transition there may be patches of oxide still in their first cycle of growth and patches which have passed through transition. Hereafter the sample with oxide thickness 2.25 μm will be referred to as being 'around transition'. The next two samples (3.50 and 4.05 μm oxide thicknesses) are within the second cycle of oxidation, whilst the thickest sample measured (6.17 μm) is in its third cycle of oxidation.

Blocks of approximately 8 mm x 5 mm x 20 mm were cut from the oxidised Zircaloy tiles using a precision saw. These were mounted between two solid brass horizontal cylindrical segments, with the whole assembly placed inside an aluminium tube (Figure 2). The two halves of the brass cylinder, the Zircaloy-4 block and the aluminium tube were glued together using Gatan G1 resin. This procedure enabled thin sections to be fabricated whilst maintaining the integrity of the oxide.

Discs of approximately 1 mm thickness were then cut from the central region of the assembly. These discs were ground and polished on both sides, using sequentially finer silicon carbide grinding paper, diamond suspensions on polishing cloths to 1 μm, then a suspension of colloidal silica, to achieve a mirror-finish. The final polished discs were ~0.5 mm in thickness.

Table 1   Comparison of effective oxide thicknesses as determined by XRD from the FWHM of the entry-exit curves with oxide thicknesses determined by weight gain.

Sample Identifier (Oxide thickness by weight gain)	Description	Effective oxide thickness by XRD (µm)
0.46 µm	1st cycle	0.65
1.13 µm	1st cycle	1.56 1.58
2.09 µm	1st cycle	2.21 2.12
2.25 µm	Around first transition	4.13 3.48
3.50 µm	2nd cycle	3.80 3.88
4.05 µm	Later in 2nd cycle	5.10 4.91
6.17 µm	3rd cycle	6.43 6.39
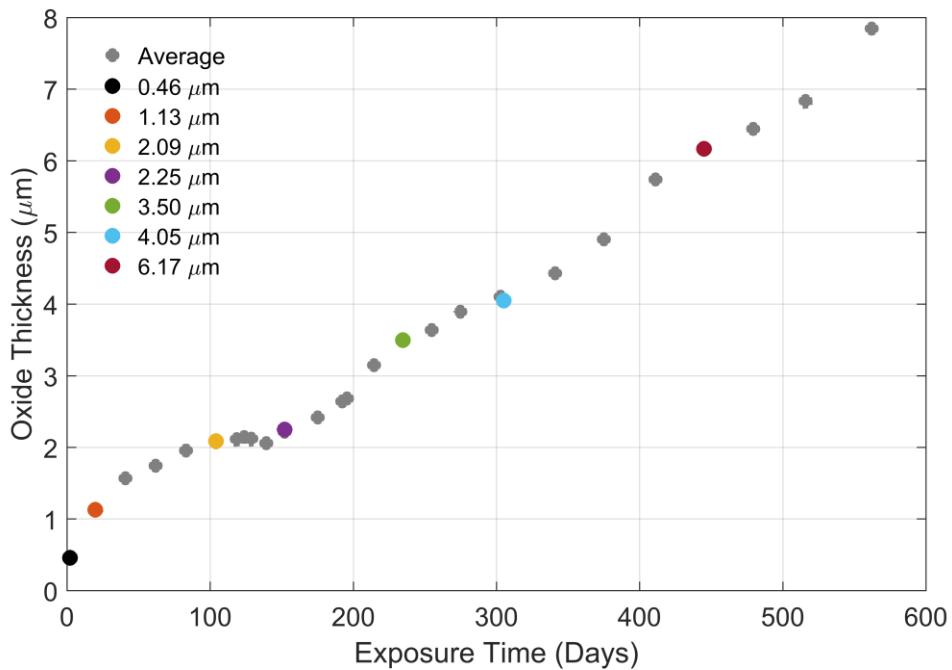
Figure 1   Oxide thicknesses (obtained via weight gain measurements) versus oxidation time: average oxide thickness data from a batch of 28 specimens, and specific oxide thicknesses of the samples selected for synchrotron XRD experiments.
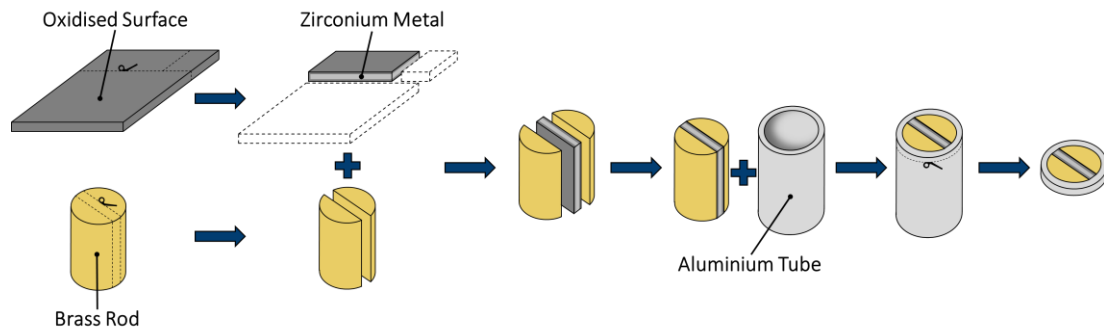
Figure 2   Schematic of the assembly used for sample preparation, showing a sample held in brass and aluminium tubes.

2.2. Nano-Beam X-ray Diffraction

Transmission X-ray measurements were performed using the nano-resolution station on the ID11 beamline at the European Synchrotron Radiation Facility (ESRF) in Grenoble, France [24]. The beam size (full-width at half-maximum) used for the experiments in this paper was ~200 nm vertically (in the oxide growth direction), and 40-50 μm horizontally, thus allowing the measurement of through-thickness spatially resolved diffraction patterns in Zircaloy-4 oxides which are only a few micrometres in thickness. This beam geometry and the sample thickness mean that a slight angular deviation could result in the beam sampling significantly more than 200 nm in the vertical direction. The sample was therefore carefully aligned to ensure parallelism of the X-ray beam with the oxide interface in both the beam direction and perpendicular to the beam direction. Good alignment is subsequently demonstrated in the results for both stresses and phase fractions that show clear modulations with oxide depth.

An X-ray energy of ~65 keV was selected in order to ensure penetration of the 0.5 mm thick sample of Zircaloy / Zircaloy oxide. The sample to detector distance of ~500 mm was chosen to allow whole Debye-Scherrer rings with radii up to $2\theta = 5.8°$ to be measured. This encompassed all the significant low-angle Bragg reflections from both the monoclinic and tetragonal oxide and the Zircaloy-4 metal. To confirm, a reduced detector distance (~350 mm) was selected for one-sample (2.25 μm oxide) which increased the angular range and no additional significant reflections were observed.

Each Zircaloy oxide sample was attached to a glass slide, together with a powdered ceria standard reference material (for calibration purposes), and mounted on the sample stage. The top surface of the oxide (brass-oxide interface) was aligned with the beam, and the polished face of the oxide (cross-section) was made perpendicular to the beam direction. Several series of diffraction patterns were then recorded per sample, using a counting time of 10 seconds per diffraction pattern and a vertical step-size of 50 nm. The range of each series of diffraction pattern acquisitions in the vertical direction was such that it encompassed the Zircaloy oxide and included a portion of both the brass mounting material and the Zircaloy metal substrate, which sandwiched the oxide of interest. Between each data series the sample was either tilted around the horizontal axis perpendicular to the beam direction (to provide a measure of the sensitivity to this rotational alignment), or moved laterally by several hundred micrometres (in order that a different section of the oxide could be investigated without significantly altering the alignment).

A series of diffraction patterns was also collected from the cerium dioxide powder, in order to calibrate the sample-detector distance and detector non-orthogonality. The ceria diffraction and 'dark-field' images (in the absence of the X-ray beam to account for any background or noise picked up by the detector) were obtained each time a sample was changed.

3. Data Analysis

Key parameters from the calibration data were calculated using Fit2D [25,26,27] directly. The later stages of the data reduction (integration of the sample data), refinement of structural models from diffraction patterns, phase fraction and stress calculation stages of the analysis were all performed with bespoke functions written using MathWorks Matlab 2014b, and calling on specialist programs where required, as detailed in the following paragraphs.

3.1. Data Reduction

The sample data, comprising Debye-Scherrer ring patterns imaged by the detector, were corrected for the offset in beam centre position, detector non-orthogonality and the spatial distortion of the detector (calculated from the diffraction data for the cerium dioxide standard) using Fit2D. In addition, the dark-field images were subtracted, in order to account for electrical background noise on the detector. Tables of intensity (arbitrary counts) versus 2θ (obtained via knowledge of the sample-detector distance as calculated from the cerium dioxide analysis) were output firstly for a full 360° azimuthal integration, and secondly for 36 azimuths to produce datasets integrated over 10° sectors around the diffraction pattern. Each dataset was then normalised to account for actual X-ray intensity (which decreases with the decreasing synchrotron storage ring current between top ups).

3.2. Rietveld Refinement of Structural Models

3.2.1. Calibration of Instrument Broadening

The experimental set-up (beam and detector) will introduce a zero offset and contribute to peak broadening. Parameters to describe these were determined by analysing the ceria standard. The ceria diffraction patterns were firstly corrected for dark-field, spatial distortion, detector non-orthogonality and beam centre position. The program 'Bruker DiffracPlus TOPAS v4.2' was used to refine a structural model of the ceria, using the Rietveld method [28], a Thompson-Cox-Hastings pseudo-Voigt type profile [29] and the structural parameters found in [30,31,32]. The lattice parameter and crystallite (or domain) size for the structure were fixed to that given by the standard [33], whilst all other parameters (zero error, background, scale, peak profile parameters) were allowed to refine. The resulting zero offset and peak profile parameters were recorded and used in the subsequent Rietveld refinements of models of the Zircaloy oxide sample data. Any remaining peak broadening or change in peak shape could then be attributed to properties of the sample (for example, strain and/or grain size).

3.2.2. Sample Diffraction Patterns for Zircaloy Oxide

Firstly, a representative diffractogram containing all possible phases in the Zircaloy, Zircaloy oxide and mounting material was chosen to provide the initial (or 'seed') fit in TOPAS. Inclusion of the mounting material is important since the beam tails are long, compared to the full width at half-maximum of the beam, and can therefore give rise to diffraction from regions outside the FWHM of the beam. The diffraction from the mounting is notable, so its inclusion is important in simulating the complete pattern over the chosen range of 2θ. The initial structural details for each phase were taken from [34,35,36,37,38,39], including the atom sites, occupancy, isotropic temperature factors, space groups and lattice parameters. The phases comprised:

- Monoclinic ZrO_2 [34]
- Tetragonal ZrO_2 [36]
- Hexagonal close-packed α-zirconium [35]
- Face-centred cubic α- and body-centred cubic β'-brass (from the mounting material) [37,38]

- Face-centred cubic lead (a machinability additive to the brass) [39].

The diffraction patterns of the Laves phase and ZrO suboxide were also considered but deemed not to be required, due to the contribution to the overall diffractogram being very small, or the significant peaks being present outside of the measured 2θ range. 21 Bragg reflections from the monoclinic oxide, 4 from the tetragonal oxide and 3 from the zirconium substrate were within the region of the diffractogram analysed here. It should be noted that the Rietveld analysis did not show any significant residual crystalline peaks once the above structures were accounted for.

The Rietveld methodology [28] was selected to ensure the highest degree of structural relevance for each phase and to allow for deconvolution of overlapping peaks. Additional Gaussian or Lorentzian functions within the model were enabled as required to accommodate any material-related peak broadening.

The textures of the monoclinic oxide and the Zircaloy metal were accounted for by using preferred orientation functions. For the tetragonal oxide model, where only one tetragonal peak is isolated from other phases (the others being combined with monoclinic or matrix reflections), no preferred orientation term was used.

Rietveld refinement of the model was then performed for all the diffractograms in each series. Phase weight fractions for each of the six phases were calculated from the full 360° azimuthally-integrated data. Refined lattice parameters were output for each 10° azimuthal integration, and were subsequently used to calculate the interplanar spacings for the $\{11\bar{1}\}_m$ monoclinic and $\{101\}_t$ tetragonal planes.

3.3. Entry-Exit Curves and Phase Fractions

The location of the oxide was determined by plotting the total oxide phase fraction as a function of the vertical position of the sample. The total fraction of oxide was calculated as the sum of the monoclinic and tetragonal oxide phase fractions calculated as described above for the full 360° azimuthally integrated datasets for each specimen displacement (depth into the oxide). The calculation of phase fractions for all components of the diffraction pattern (brass mounting, oxide and metal) is necessary to determine interchange between discrete regions of the assemblage (mounting to oxide and oxide to Zircaloy metal). The resulting plot (Figure 3) represents the oxide layer's entrance into, and exit from, the X-ray beam as the sample is translated across the beam, and is termed an 'entry-exit curve'. The FWHM provides a measure of the oxide thickness. The total oxide weight fraction is always below 100% since the tails of the beam give rise to brass mounting and Zircaloy metal reflections within the diffractograms, even when the beam is focussed on the centre of the oxide. Similarly, when the beam is in either the Zircaloy metal or brass mounting, the tails interact with the oxide volume. This yields signal from the monoclinic and tetragonal phases, providing the minimum oxide fraction within the diffractogram.

When the phase make-up of the oxide was considered, the tetragonal phase fractions were calculated as a proportion of the sum of monoclinic and tetragonal oxide phases only. As 360° azimuthal integrations were used, diffraction from planes oriented towards both the in-plane and through-plane directions (and all intermediate angles) was sampled. Under the assumption that both in-plane directions are equivalent, this should make an evaluation of phase fraction performed in this way insensitive to any changes in texture that may occur as a function of position within the oxide. In addition, Garner et al. [20] found no orientation relationship between the tetragonal oxide crystallites and the metallic substrate, suggesting an effectively random texture. This can be seen in the orientation of tetragonal crystallites presented in Fig. 9(a) in that work, where no spatial relationship is apparent within the oxide.
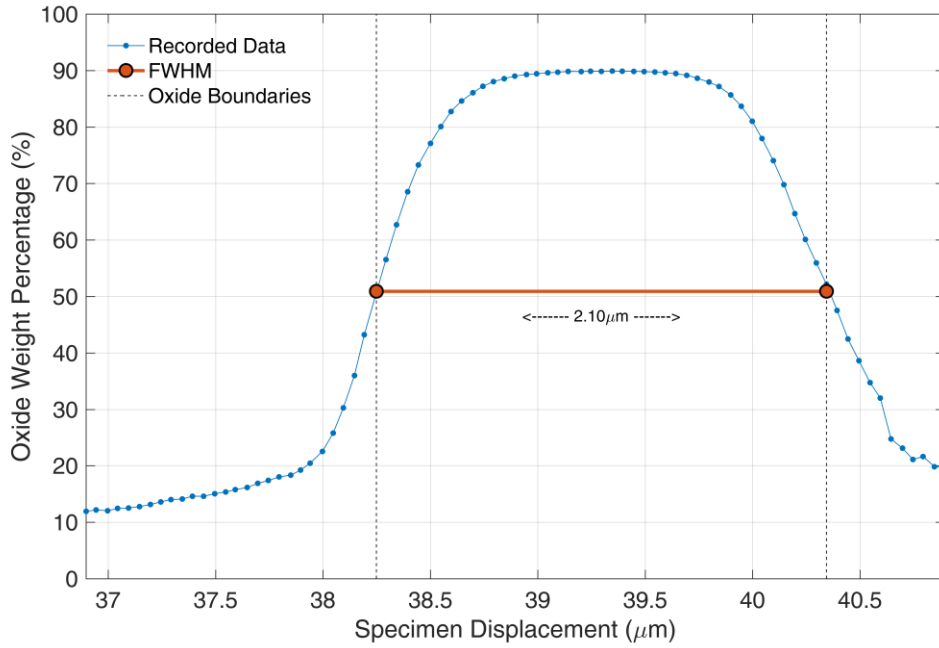
Figure 3   **Example oxide entry-exit curve showing how the nominal start and end of the oxide is determined from the FWHM.**

3.4. Calculation of Oxide Residual Stress

The presence of strain within either Zircaloy oxide phase will give rise to a shift in the diffraction peak positions from their unstrained position, according to Equation 1.

$$\varepsilon_\psi = (d - d_0)/d_0$$

Equation 1

Here, ε is the strain in a given direction ψ, d is the measured interplanar spacing and d_0 is the unstressed interplanar spacing. Since the diffraction patterns measured on beamline ID11 comprise whole Debye-Scherrer rings, the strains in two orthogonal directions can be measured. The angle ψ is measured relative to the surface normal of the Zircaloy oxide layer, and equates approximately to the angle around the measured Debye-Scherrer rings. The diffraction peaks measured at 0° and 180° (corresponding to the north and south compass points of the diffraction rings respectively) are shifted from their unstressed positions according to the near through-plane strain. The diffraction peaks measured at 90° and 270° (corresponding to the east and west compass points) will be shifted according to the sample's in-plane strain. Therefore, if the sample exhibits different strains in the through-plane and in-plane directions, the diffraction rings will be elliptical. Diffraction peaks recorded at the intermediate ψ angles (between the compass points) will be shifted according to a strain that is a tensor sum of the strains in the in-plane and through-plane directions.

Under the assumption that the in-plane stress is equal in both in-plane directions, the interplanar spacing measured in a given direction, ψ, is given by triaxial stress theory as Equation 2 [40,41].

$$d_\psi = d_0 \left(\frac{1+v}{E}\right) \left[\sigma_{in-plane} - \sigma_{through-plane}\right] \sin^2 \psi$$
$$+ d_0 \left(\frac{\sigma_{through-plane} - 2v \cdot \sigma_{in-plane}}{E} + 1\right)$$

Equation 2

In this expression, d_ψ is the interplanar spacing in the direction ψ, d_0 is the unstressed interplanar spacing, $\sigma_{in-plane}$ and $\sigma_{through-plane}$ are the in-plane and through-plane stresses, respectively. The parameters E and v are the Young's modulus and Poisson's ratio, respectively, for the $\{11\bar{1}\}_m$ reflection, and are taken from [5]. Identical elastic constants were used for the $\{101\}_t$ reflection (as in [5], due to the lack of reliable data for the tetragonal phase at room temperature).

A plot of the values of d_ψ versus $\sin^2\psi$ at a given depth in the oxide is expected to give a linear relationship. The gradient and intercept terms form a pair of simultaneous equations, from which any two of the three unknown parameters (d_0, $\sigma_{in-plane}$ and $\sigma_{through-plane}$) may be extracted. The boundary condition that the through-plane stress must be equal to zero at a free surface can be applied to the data from zero oxide depth, and hence values for d_0 and $\sigma_{in-plane}$ calculated. At greater depths, additional assumptions must be made. If the through-plane stress is assumed to be zero at all depths, d_0 appears to modulate with oxide depth, as shown in [16]. Conversely, if d_0 is assumed to be constant with depth, then the effects of changes in stoichiometry must be ignored. The oxide is expected to become increasingly sub-stoichiometric with distance from the oxide surface, which would produce a monotonic change in d_0 with depth. Since the observed modulations were not monotonic, it appeared that the effects of stoichiometry changes were smaller than effects of through-plane stresses. The unstressed interplanar spacing, d_0, is therefore assumed to be constant with oxide depth [42] thus enabling the calculation of $\sigma_{in-plane}$ and $\sigma_{through-plane}$ at all other depths in the oxide. Although stoichiometry effects have been excluded, relative trends identified in stresses should remain valid.

The lattice parameters calculated from the structural models of the monoclinic and tetragonal oxide phases for each 10° azimuthal integration were used to calculate the interplanar spacings (d_ψ) for the $\{11\bar{1}\}_m$ and $\{101\}_t$ planes [40]. A 'Bisquare Weightings' method of linear regression was used to analyse the relation between interplanar spacing and $\sin^2\psi$ (in order to reduce the effect of any outliers on the linear fit). The resulting gradient and intercept values were used in the calculation of the $\{11\bar{1}\}_m$ monoclinic and $\{101\}_t$ tetragonal unstressed interplanar spacings and in-plane stresses at the oxide surface, and the in-plane and through-plane stresses throughout the oxide. The uncertainties in the reported stress values were calculated from the uncertainties in the gradient and intercept.

4. Results

4.1.　Effective Oxide Thicknesses Obtained from XRD Data

The entry-exit curves for all the samples, offset horizontally such that the nominal start of each oxide is at 0 μm on the x-axis (oxide depth), are shown in Figure 4. The 'effective oxide thicknesses', derived from the FWHM of the entry-exit curves, are listed in Table 1, together with weight gain measurements.
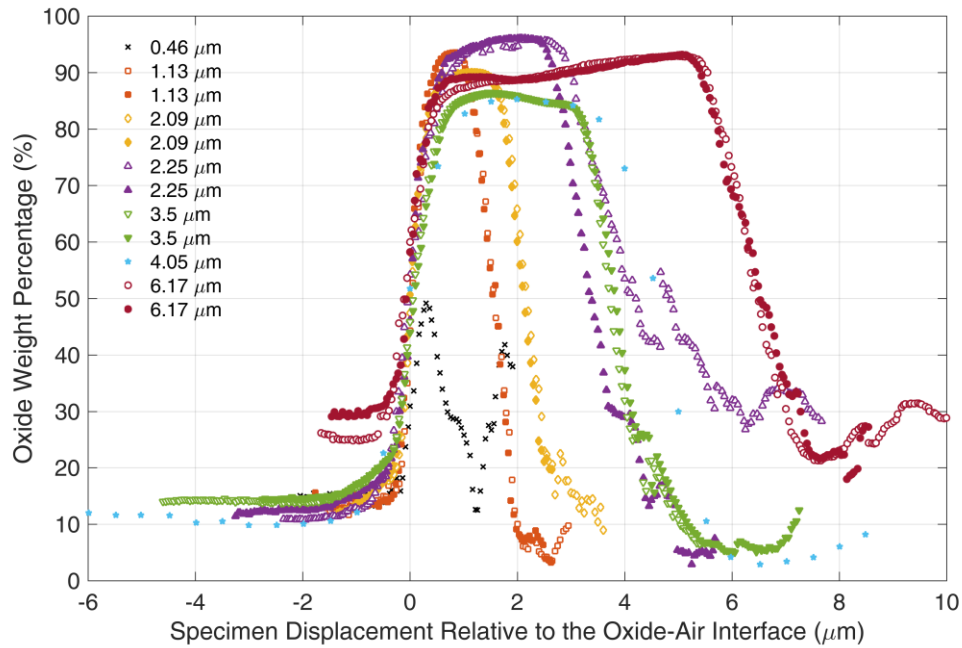
Figure 4   Oxide entry-exit curves for all samples, offset such that the nominal surface of the oxide is at 0 μm depth.

The effective oxide thicknesses as measured from the XRD entry-exit curves are slightly larger than those obtained via weight gain, since imperfect alignment will result in an overestimate of the oxide thickness by the XRD method. In all following figures in this paper, therefore, the x-axes are proportionally scaled such that the FWHM of the entry-exit curve is set to be equal to the average oxide thickness as measured by weight gain. Zero depth into the oxide represents the nominal location of the air-oxide interface (or brass-oxide interface once mounted), and the maximum oxide depth shown in all figures corresponds to the oxide-metal interface region.

It should be noted that data from the thinnest sample (0.46 μm) were challenging to analyse due to the small oxide thickness with respect to the vertical beam size, and the likelihood of a large strain gradient. For these reasons, the initial or 'seed' TOPAS fit was specifically tuned for this complex sample, and parts of the diffraction pattern were necessarily excluded to enable reliable Rietveld refinement. Regardless of this, four monoclinic reflections (including $\{11\bar{1}\}_m$) and the main tetragonal reflection ($\{101\}_t$) were included when analysing the 0.46 μm oxide, ensuring that the resulting tetragonal phase fractions were comparable with those from the thicker oxides for which the whole of the measured 2θ range could be fitted.

4.2.   Stress Distributions – Monoclinic Phase

The in-plane and through-plane stress distributions with depth into the oxide, generated from the $\{11\bar{1}\}_m$ monoclinic oxide peak, are shown in Figure 5, demonstrating consistency between repeated measurements. The uncertainties in the stress profiles are shown in Figure 6. Modulations in the stresses with depth into the oxide (which are greater than the uncertainty associated with each stress calculation) can be clearly observed for the thicker samples. In samples (not included in this work) with poor alignment of the oxide with the incident beam, stresses are averaged over a range of depths within the oxide and these modulations are flattened. The presence of stress modulations in the data presented here indicates that the samples are sufficiently well aligned for real trends in the stress distributions to be discerned.
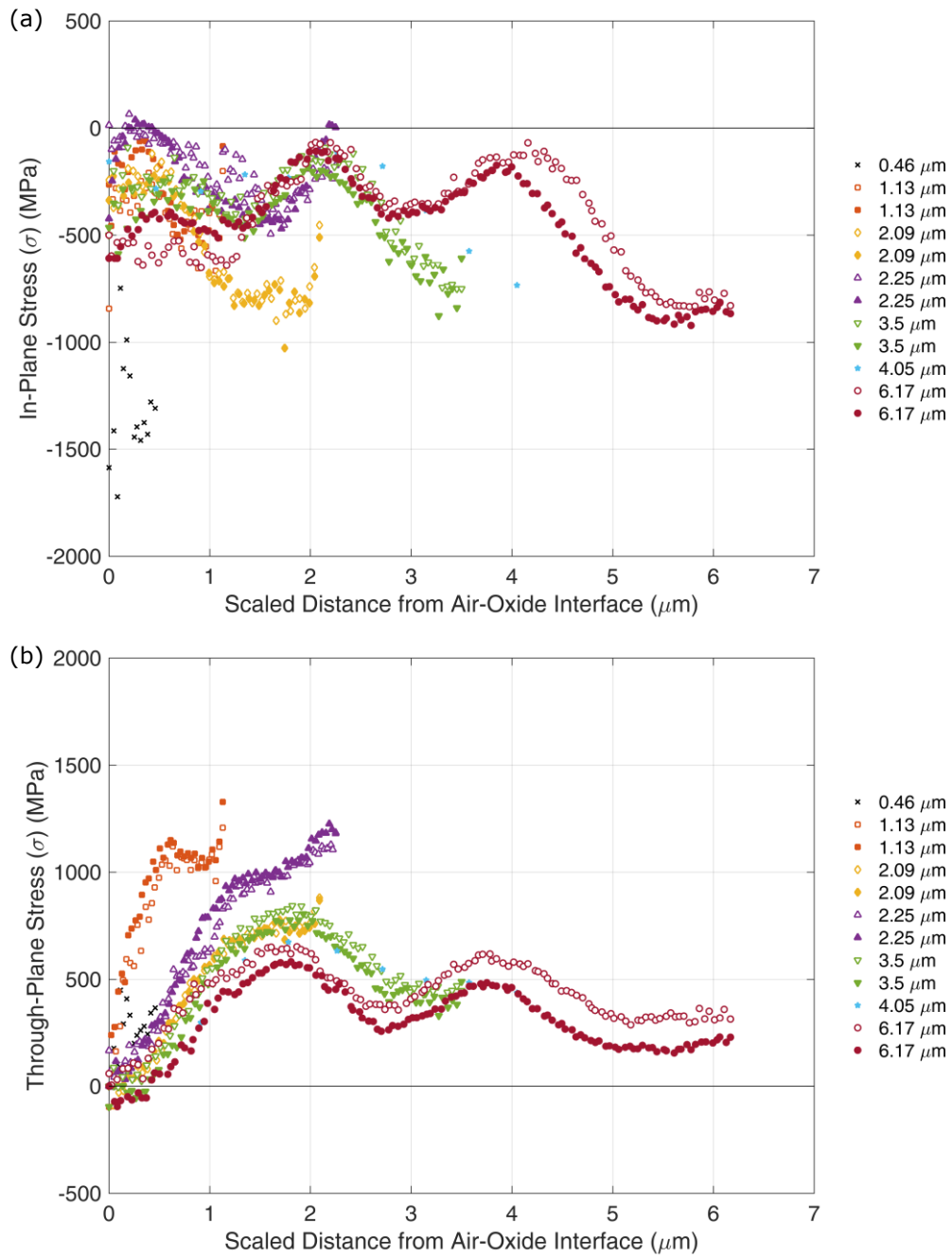
Figure 5 Monoclinic oxide stress distributions: (a) in-plane stress, (b) through-plane stress.
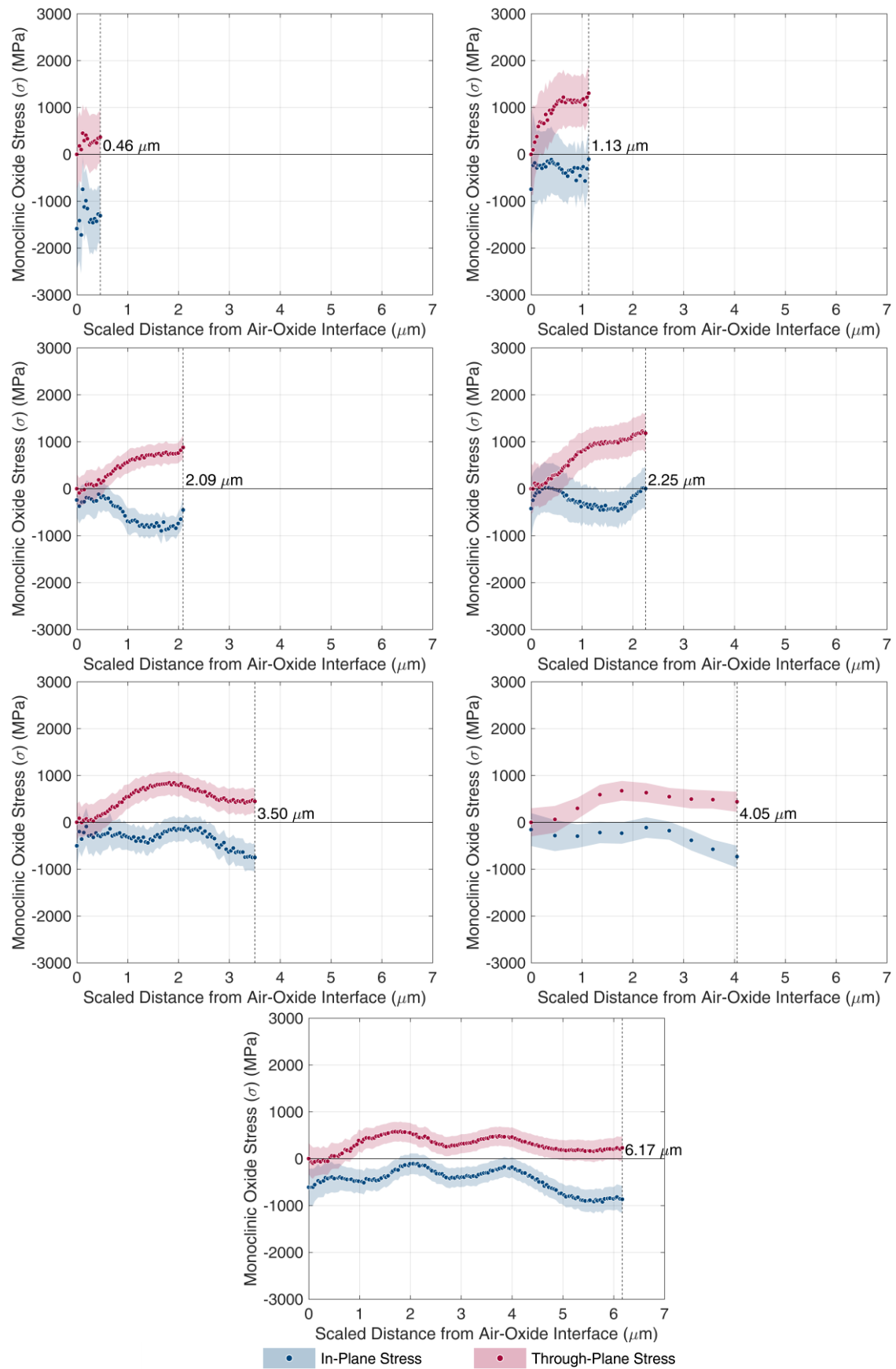
Figure 6 Calculated uncertainties for the monoclinic oxide stress profiles, with shading representing one standard deviation.

4.2.1. In-Plane Monoclinic Stress

The in-plane monoclinic oxide stresses are highly compressive in the thinnest (0.46 μm) oxide. Comparison with data from thicker oxides shows that the stress in this first ~0.5 μm has relaxed significantly by the time the oxide reaches a thickness of ~1 μm and remains low thereafter.

Beyond the outer 0.5 μm, the stresses become more compressive up to a depth of 1-1.5 μm, whereupon the stress distribution levels off (in the case of the 2.09 μm thick oxide), or again diminishes to around zero (in the case of the 2.25 μm thick oxide). This progression of increasing and decreasing compressive in-plane stress is repeated in the subsequent oxide grown in the second and third cycles.

4.2.2. Through-Plane Monoclinic Stress

The through-plane stress in the monoclinic oxide is low, but slightly tensile, in the thinnest (0.46 μm) oxide. By the time the oxide has grown to a thickness of ~1 μm, the through-plane stress is then observed to become more tensile, whilst being constrained to zero at the outer surface. In the first cycle oxides, the through-plane stress tends to plateau near the metal-oxide interface (mirroring the in-plane stress). In the case of the 2.25 μm thick oxide (near transition), the through-plane stress continues to increase up to the metal-oxide interface, whilst for the post-transition oxides, the through-plane monoclinic stresses show repeated patterns of increasing and decreasing tensile stress with depth into the oxide.

4.3.   Stress Distribution – Tetragonal Phase

The in-plane and through-plane stress distributions for the tetragonal phase with depth into the oxide are shown in Figure 7. The in-plane stresses for the tetragonal phase exhibit more series-to-series variability for a given sample than the monoclinic oxide in-plane stresses, which may be expected given the relatively low signal from the $\{101\}_t$ diffraction peak. Even so, it is possible to observe trends both with oxidation time and with depth into the oxide.

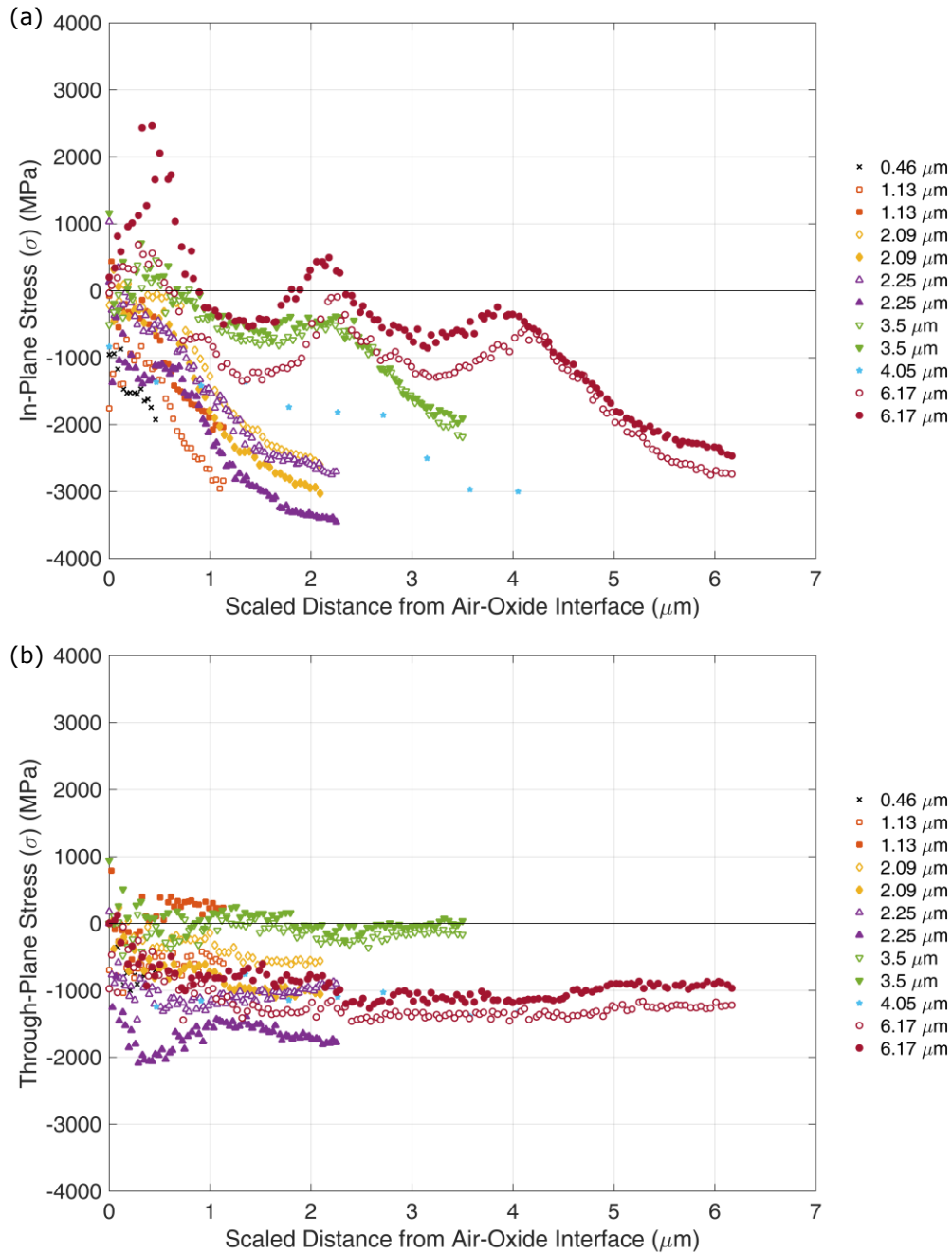### 3.2.1. In-Plane Tetragonal Stress
Similarly to the monoclinic in-plane stress distributions, the in-plane tetragonal stresses are mostly compressive, although their magnitudes are much greater, reaching -3500 MPa rather than -1600 MPa. In the pre-transition oxides, the stresses become gradually more compressive with depth, and unlike their monoclinic stress distribution counterparts, do not exhibit any stress relaxation up to the metal-oxide interface. After each transition, however, the stresses in the fossil oxides formed in earlier cycles relax considerably and even become slightly tensile both near the oxide surface and at a depth of ~2.1 μm for the third cycle oxide (6.17 μm oxide thickness). The stress profiles for the second and third cycle oxides then show qualitatively similar trends to the equivalent monoclinic in-plane stress profiles, with increasing compression in the first half of each cycle, followed by stress relaxation in the latter half.

It is clear, however, that the in-plane stress at any location also gradually diminishes over time. In the thinnest sample (0.46 μm), large in-plane stresses are apparent at the oxide surface, which decrease significantly with further oxide growth, becoming slightly tensile in places for the third cycle oxide.

4.3.2. Through-Plane Tetragonal Stress
The through-plane tetragonal stresses are mostly compressive; therefore, unlike the monoclinic grains, the tetragonal grains encounter some degree of hydrostatic compression. There is significant sample-to-sample variation; however, unlike the stress

distributions described previously, the through-plane tetragonal stresses do not modulate significantly with depth into the oxide.

Figure 7   Tetragonal oxide stress distributions: (a) in-plane stress, (b) through-plane stress; note that filled and non-filled symbols correspond to separate data sets acquired from the same sample.

4.4. Tetragonal Oxide Phase Fraction

The distribution of the tetragonal oxide phase fraction (as a proportion of the total oxide) is shown in Figure 8. For all the samples, the tetragonal phase fraction reaches a maximum near the metal-oxide interface. In several samples, there is also a relatively high level near the specimen surface, although there is some variability in this region. At

14

any other location, the tetragonal phase fraction clearly decreases progressively with time. In the older, post-transition oxides, the tetragonal phase fraction in regions away from the interfaces appears stable around 5-8%. Within this range, the post-transition samples exhibit repeating patterns of increasing and decreasing tetragonal phase fraction, similar to the behaviour of the monoclinic and tetragonal in-plane stresses.
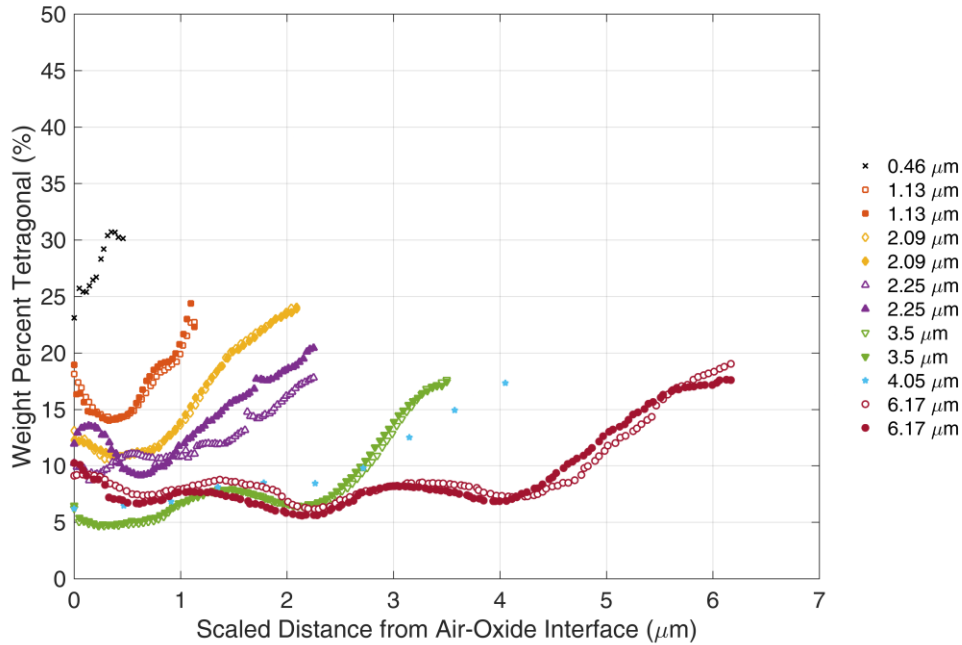
Figure 8   Distribution with oxide depth of the weight percent of tetragonal oxide phase.

5. Discussion

Nano-focus transmission XRD has been used to investigate the monoclinic and tetragonal residual stress profiles and tetragonal:monoclinic phase fraction distributions with oxide depth, for Zircaloy oxides within the first three cycles of oxide growth. This method yields spatially-resolved measurements, and does not average over a large oxide depth or rely on complex deconvolution methods. In conjunction with Rietveld model refinement, it has been possible to discern non-monotonic changes in the stress profiles for both oxide phases. This is in contrast to previous single reflection analysis [16] in which the monoclinic stress profiles were attainable from the position of the strong, isolated $\{11\bar{1}\}_m$ peak, but the tetragonal stress profiles were subject to significant uncertainty due to significant peak overlap and the low tetragonal phase fraction, and as such, showed no consistent trends with depth or oxidation history.

The changes in the stress profiles and tetragonal phase fraction distributions with exposure time are discussed here in relation to the typical oxide morphology [16,43,44] and together, the observations are used to construct a mechanism for transition which is consistent with the observed trends.

5.1.   Mechanisms of Stress Relief

The measured stress distributions are discussed here in relation to the mechanisms of stress relief and the associated oxide morphology, as described in [16]. These stress relief processes are significant because they result in cracks that ultimately combine to produce percolation paths for the pressurised water to reach the metal-oxide interface directly,

thus allowing the reaction to form ZrO_2 to take place once again at an accelerated rate (transition).

5.1.1. In-plane stress

Zirconium alloys oxidise by the inward diffusion of oxygen, thus the formation of oxide is associated with material expansion which, constrained by the underlying metal produces compression in the oxide balanced by tension in the metal. The highest compressive in-plane stresses measured in the present work were in the thinnest oxide (0.46 µm), with consistently large values near the metal-oxide interface. As the oxide grows, the stress diminishes in the first 0.5 µm from the outer surface, leaving very little compression close to the outer surface by the time the oxide is 2.25 µm thick. In the thicker pre-transition oxides, the compressive stress tends to increase at depths greater than 0.5 µm below the surface (Figure 5 and Figure 6).

The early appearance of the stress relief and the through-oxide trend in stress suggest that newly formed oxide is highly compressed and that a continuous stress-relief process is operating throughout each cycle of oxidation. The most likely candidate for this process is the plasticity observed to be induced in the metal ahead of the moving oxidation front. TEM shows evidence of markedly increased dislocation density in the previously annealed metal, even ahead of the 0.46 µm oxide in this program [16]. Both dislocations and cell boundaries have been observed ahead of thicker oxides in other alloys [45]. Since the plastic layer is present at all oxide thicknesses, it must be continuously reformed as the oxide consumes the metal, i.e. as each new plane of metal is oxidised, it renews the tensile stresses in the metal ahead of the interface, producing an increment in plastic strain in the metal substrate.

The increment of metal strain relaxes both the tensile stress in the metal and the compressive stress in the newly formed plane of oxide. It also adds a small tensile component to the strains in all older portions of the oxide. As the interface progresses, the increments sum, and the overall loss of compression is thus greatest in the oldest portions of the oxide. This produces the gradient in compressive stress between the surface and ~1 µm. The particularly significant aspect of this mechanism is that stress changes in the oxide are a by-product of a process in the metal at the moving interface. There is, thus, no reason for the increments to stop once the compressive stress in the oxide is relieved. In this aspect, the process is unlike a stress-relieving mechanism based on oxide behaviour alone.

The monoclinic stresses, as measured at room temperature over the first ~0.5 µm nearest the oxide surface, reach zero as transition is approached. Experimental measurements of the temperature-induced stress change in monoclinic zirconia show that with increasing temperature, the stress becomes less compressive, although estimates of its magnitude vary [46]. Consideration of the thermal expansion, therefore, gives rise to the possibility that the near-surface stress in the sample just prior to transition was, in fact, slightly tensile at the oxidation temperature of 350°C. Tensile stresses in the oxide could not have been produced by a stress relief process based on oxide properties alone, but could be induced by the accumulated effects of plasticity in the metal. As the interface moves inwards, incremental strains in newly stressed metal lead to accumulated strains in the older portions of the oxide that can become tensile.

In the thicker pre-transition oxides, the monoclinic in-plane stress profile exhibits a flattening off around 1 µm below the surface, coinciding with the growth of interfacial undulations (Figure 9). The undulations result from random protrusions in the growing interface, which are then stabilised by the local reduction in the in-plane stress mismatch between the oxide and the metal. The stress redistribution associated with the undulations leads to tensile through-plane stresses near the interface, as previously calculated by Parise et al. [47], and to the nucleation of lateral cracks at the delays in the oxidation front.

As the interface moves inwards, the small lateral cracks left behind experience the bulk in-plane compressive stress. This allows the cracks to open out (Figure 9), such that they

become increasingly linked and form a 'band' of lateral cracks, giving rise to the additional stress relief in this region. The importance of interfacial undulations and lateral cracks in relieving stress is in accordance with calculations by Platt et al. [13], who used finite element analysis to model the effect of oxide creep, metal creep and hydrogen-induced lattice strain on the oxide stress distribution. Those authors concluded that these factors were not sufficient to explain the observed stress relaxation with increasing exposure time, and therefore that other mechanical degradation mechanisms were likely to play a role.

As the pre-transition oxide grows further, the monoclinic in-plane stress at the metal-oxide interface reduces significantly, reaching zero for the sample around or just prior to transition. As discussed for the near-surface stresses, this measurement of zero stress at room temperature could correspond to a tensile stress near the metal-oxide interface at elevated temperature.

The possibility of tensile stresses near the outer surface and the metal-oxide interfaces is important because such stresses could explain (i) the high-resolution SEM observations of extended through-plane cracks running inwards from the surface, and (ii) TEM observations of fine intergranular through-plane cracks running from the tips of lateral cracks to the metal-oxide interface, in the 2.25 μm thick Zircaloy-4 oxide [16]. These cracks were in the through-thickness plane rather than at 45° to it, as would be seen if cracking occurred under a compressive in-plane stress. Given the progression of the stress distributions between the 0.46 μm film and the 2.25 μm film, it is feasible that with a few additional days of oxidation, and at the oxidation temperature [47], compression could be lost across the entire oxide film, and the near-surface and near-interface cracks could link up. This would explain the through-thickness cracking observed via high resolution SEM and nano-SIMS [60]. It could also explain more generally why porosity observed in the TEM (e.g. [1] and [48]) links along the through-thickness direction rather than along other paths.
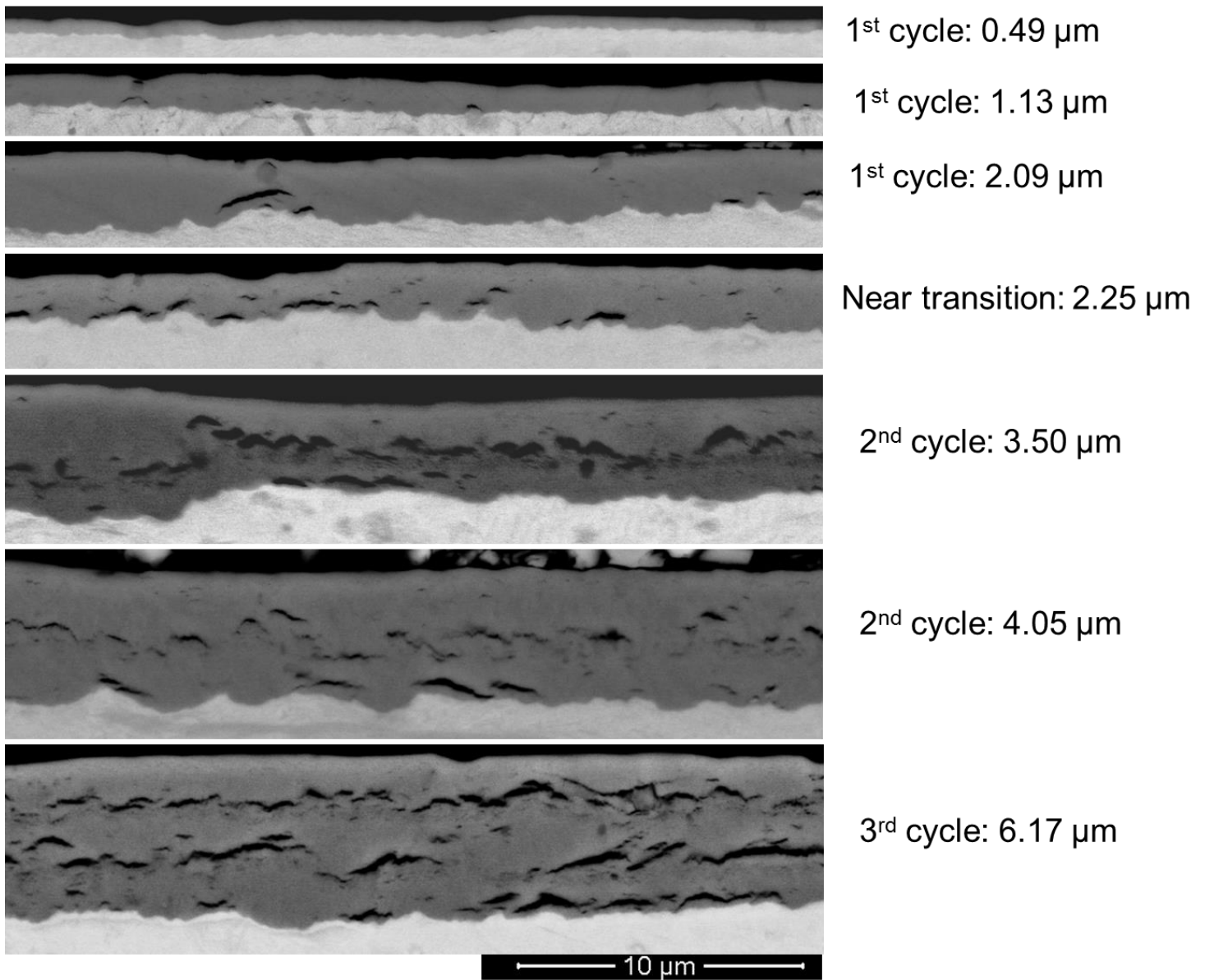
An additional source of overall stress relief in the oxide comes from the tetragonal to monoclinic phase transformation. The volume and shape change associated with the transformation of a tetragonal grain [49] induces localised regions of both tensile and compressive stresses in the surrounding monoclinic material. These superpose onto the background compressive field. The initial phase transformation may occur as a newly nucleated grain at the metal-oxide interface grows beyond a critical size. This happens at all times (regardless of a sample's proximity to transition), thus leaving behind a mosaic of stress variations. Transformations may also be stress-induced, occurring in the tensile field at delays in the oxide front, and/or as the bulk prevailing compressive stress reduces, for the reasons already discussed. Finally, the transformation stress from an initial transforming grain may reduce the compression on nearby tetragonal grains, thus encouraging further transformation and increasing the local variation in stresses. The stresses in the tensile regions around the transformed grains may be sufficient to nucleate small cracks immediately after the transformation, but such microcracks will not be able to extend once they run into the surrounding compressive field. The background compressive stresses must reduce before the microcracks can link.

In the post-transition samples, the stress distributions are non-monotonic. The repeated regions of increasing compressive stress with depth observed for the 3.5 μm oxide sample (second cycle), and for the 6.17 μm oxide sample (third cycle) coincide with the oxide portions formed just after each transition which contain no lateral cracks. The progressive reduction of the oxide stresses (both with time, and with distance from the metal-oxide interface) is therefore again likely to be associated with deformation of the underlying metal.

The subsequent flattening-off and relaxation of the stresses with depth for samples with oxide thicknesses of 4.05 μm and 6.17 μm, respectively, are also a repeat of the flattening-off and relaxation occurring in the first cycle. This is likely to be the effect of the development of a second band of lateral cracking (as shown via SEM in Figure 9 and in [43] for Zircaloy-4 oxides formed under similar conditions).

This can be seen in Figure 10, where a micrograph of the 6.17 μm oxide sample is superposed with the in-plane stress distribution. In this figure, it is evident that bands of cracking correspond with reduced in-plane stresses, whilst regions of increasing

compressive stress are those where cracking is reduced. Although the micrograph shows specific microstructural features in a single image and single grain (whereas X-ray derived stresses constitute bulk measurements), it should be noted that this micrograph is typical in terms of the depth locations for the bands of lateral cracking.

1st cycle: 0.49 μm

1st cycle: 1.13 μm

1st cycle: 2.09 μm

Near transition: 2.25 μm

2nd cycle: 3.50 μm

2nd cycle: 4.05 μm

3rd cycle: 6.17 μm

10 μm

Figure 9   SEM images of the samples studied, showing the development of undulations and isolated cracks and subsequently, bands of interlinked lateral cracking.
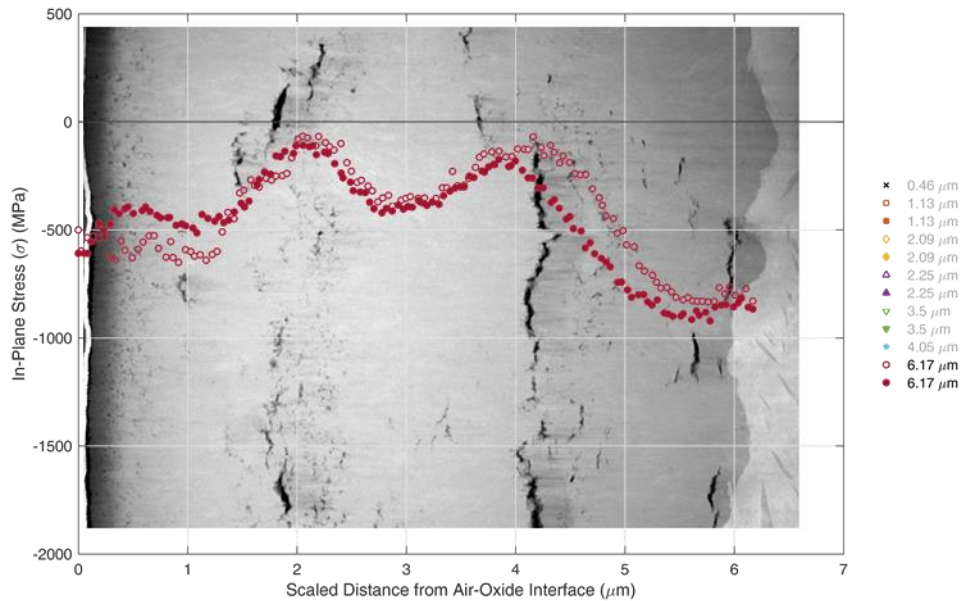
Figure 10   **Correlation between stresses determined from transmission XRD and the crack distribution observed with Scanning Transmission Electron Microscopy in the same sample.**

5.1.2. Through-Plane Stress

The monoclinic through-plane stress for the 0.5 μm oxide was measured to be near zero, as is usually assumed for thin layers. As the oxide thickens, the increase in tensile through-plane stress with depth into the oxide demonstrates that the commonly used two-dimensional stress analysis (assuming a zero through-plane stress throughout the oxide) is insufficient for oxides thicker than ~0.5 μm. It should be noted that the tensile stresses as calculated using the assumptions described in the paper are unexpectedly large for a brittle ceramic, although the trends in the through-plane stress are plausible. The high magnitudes could be due to the assumption that the unstressed lattice parameter, d_0, is a constant throughout the oxide. However, a preliminary assessment of the effect of observed redistributions of tin, iron and chromium within the oxide indicates that these factors at least will not affect d_0 in the manner required to eliminate the through-plane stress [16].

In the pre-transition samples, it is proposed that the tensile through-plane stresses near the metal-oxide interface assist with the opening out of the lateral cracks produced behind the delays in the oxide front, subsequently giving rise to through-plane stress relaxation. The stress distributions in the post-transition samples show repeated increases and decreases in the tensile stress with depth related to the periodic formation and opening out of cracks in the second band of lateral cracking.

5.2. Role of the Tetragonal Phase

The tetragonal phase has been associated with both greater corrosion resistance [12], and a higher post-transition corrosion rate [2]. It has been suggested that the higher post-transition corrosion rate, and more rapid onset of transition, is caused by cracking associated with the transformation from tetragonal to monoclinic oxide [2, 50]. However, since cracking in the oxide may also result from the presence of interfacial undulations and deformation in the metal, it is also possible that the tetragonal to monoclinic phase transformation *results* from lateral cracking and its associated stress relief, rather than being the primary cause of cracking. The roles of the tetragonal phase, including its stress

19

profiles and through-thickness distributions with oxidation history, are therefore explored in the light of observations of the oxide morphology and the monoclinic phase stress distributions determined in this work.

5.2.1. Tetragonal Oxide Stress

The magnitudes of the stresses calculated to be present in the tetragonal phase are subject to some uncertainty since the elastic constants for the $\{11\bar{1}\}_m$ plane in the monoclinic oxide have been used, but the qualitative trends are of interest. Similarly to the monoclinic stresses, the tetragonal in-plane stress shows a general reduction in magnitude with oxidation time (for any given oxide depth). This stress relief process may also be associated with the plastic deformation of the underlying metal described previously. It gives rise to tensile stresses at the oxide surface for the post-transition samples, and at a depth of ~1.9-2.2 µm (the region of oxide grown just prior to first transition) for one of the data series for the third cycle oxide, even though the data were measured at room temperature. It may therefore be possible that at the oxidation temperature, these in-plane stresses were more tensile still [46].

The trends in the pre-transition tetragonal in-plane stress profiles do not precisely emulate the pre-transition monoclinic stress profiles. Within the tetragonal grains, no stress relief is evident in the more heavily cracked region (1.4-2.1 µm) for the pre-transition samples. Two explanations for this observation are postulated here: (i) the tetragonal grains do experience stress relief, but any reduction in stress experienced by a tetragonal grain causes it to transform to the monoclinic phase. Only the more heavily compressed tetragonal grains are retained, such that the stress relaxation is not evident in the tetragonal phase information. This is entirely consistent with the evolution of the tetragonal phase fraction measured in this work, which shows that with increasing oxidation time, the tetragonal fraction decreases for any given depth into the oxide. A steady decrease of the tetragonal phase fraction (averaged through thickness) with exposure time was also observed by Zhang et al. [12] for the oxide on an NZ2 zirconium alloy. (ii) The remaining tetragonal grains do not experience marked stress relief because they may be located away from lateral cracks and grains which have undergone the tetragonal-to-monoclinic transformation, i.e. the local stress redistributions associated with these processes induce (further) transformation, so only tetragonal grains isolated from cracks and transformation stresses remain. Whatever the explanation, the difference in the stress profile trends between the tetragonal and the monoclinic grains means that it is necessary to measure the stresses in both phases in order to understand the behaviour of the tetragonal oxide rather than deduce it from the monoclinic oxide stresses alone.

Once the samples have passed through transition, stress relaxation is apparent in the remaining tetragonal grains in the fossil oxide: this occurs concurrently with a significant drop in the tetragonal phase fraction. Those grains which have transformed to monoclinic were likely to have been the larger grains, whereas those remaining as tetragonal are likely to be stabilised by a small grain size (possibly, but not necessarily, in conjunction with a smaller compressive stress). Modulations in the tetragonal stress profile occur at similar locations to those measured for the monoclinic phase, with the regions of reduced stress correlating with the locations of the bands of lateral cracking.

5.2.2. Tetragonal Phase Fraction

The trends in the tetragonal phase fraction almost mirror the trends in the tetragonal in-plane stress profiles, also showing modulations in the distribution for the post-transition samples. The tetragonal phase fraction has previously been shown not to be distributed uniformly through the oxide [51]. Polatidis et al. [5] found an overall decrease of the *average* tetragonal fraction with oxidation time. Zhang et al. [12] used grazing incidence XRD to show that for thin oxides, the intensity of the $\{101\}_t$ peak increased up to the metal-oxide interface. This was also found by Yilmazbayhan et al. [2] and by Spengler et al. [52] using micro-beam X-ray diffraction on Zr alloy cross-sections. The tetragonal phase fractions measured in this work are in agreement with [52] for thicker oxides of 12 and 39.5 µm thickness grown under similar conditions, where the maximum tetragonal

fractions of 15% and 9% were found to occur at the metal-oxide interface, and the tetragonal fraction away from this interface varied between ~3% and ~6%.

Similarly to this work, Spengler et al. [52] found the intensities of the major monoclinic and tetragonal reflections from Zircaloy-4 corrosion films to vary in-phase with depth. The periodicity of the intensity variations, and the tetragonal phase fraction plotted versus oxide depth, matched the thickness of film grown during each oxide growth cycle. Yilmazbayhan et al. [2], however, showed an out-of-phase periodicity of the $\{101\}_t$ tetragonal peak and $\{020\}_m$ monoclinic peak intensities over a depth of 20 μm in ZIRLO (several oxidation cycles), again with a periodicity similar to the oxide growth cycles.

It is well-known that the tetragonal phase is predominantly stabilised by high compressive stress. The pressure-temperature phase diagram of zirconia reported by Block et al. [53] shows that the tetragonal phase can be stabilised by hydrostatic pressures of ~3.7 GPa at room temperature, and ~3 GPa at 350°C. Arashi et al. [54], however, find the tetragonal phase to be stable only above ~430°C. Other factors such as small grain size [9,55] and the presence of alloying elements such as iron and tin [56,57,58] also affect the stability of the tetragonal phase.

The relationship between the tetragonal phase fraction and both in-plane and through-plane tetragonal phase stress in the current study is explored in Figure 11(a) and (b). It can be seen that when the magnitude of the compressive in-plane stress in the tetragonal phase is greater than ~1000 MPa, the amount of tetragonal oxide increases with compressive stress (Figure 11(a)).

The graph also shows that the amount of tetragonal phase present for a given compressive stress clearly decreases with increasing oxide thickness in the pre-transition samples. The amount of tetragonal oxide at a given stress is then higher in the thinner second cycle oxide (3.5 μm) than in the thickest pre-transition oxide (2.25 μm), decreasing again in the thicker (4.05 μm) second cycle oxide. Finally, the tetragonal content at a given stress is higher in the early third cycle oxide than in the late second cycle oxide. This cyclic trend shows that the stress is not the only phase-stabilising mechanism operating in the oxide films; grain size stabilisation is also occurring. The proportion of fine grains is greatest at the start of each cycle, so the average grain size is smallest near the start of each cycle, decreasing towards each transition. The cycling of the average tetragonal fraction at a given stress level reflects the average grain size behaviour, showing the importance of both grain size and compressive stress in stabilising the tetragonal phase.

The highest tetragonal phase fraction is ~25-30%, for in-plane stresses between -1500 and -3000 MPa. These high compressive stresses are recorded at the metal-oxide interface, and are of a similar magnitude to the through-thickness averaged tetragonal stresses reported for a thin (~1 μm) Zircaloy-4 oxide in [5]. When the in-plane tetragonal stresses are less compressive than -1000 MPa, the amount of tetragonal oxide tends to remain constant at a few percent (albeit with some sample-to-sample variation), regardless of the value of the stress, indicating that these tetragonal grains are stabilised by some other mechanism (e.g. small grain size). There is no obvious correlation between the tetragonal phase fraction and the tetragonal through-plane stress (Figure 11(b)).
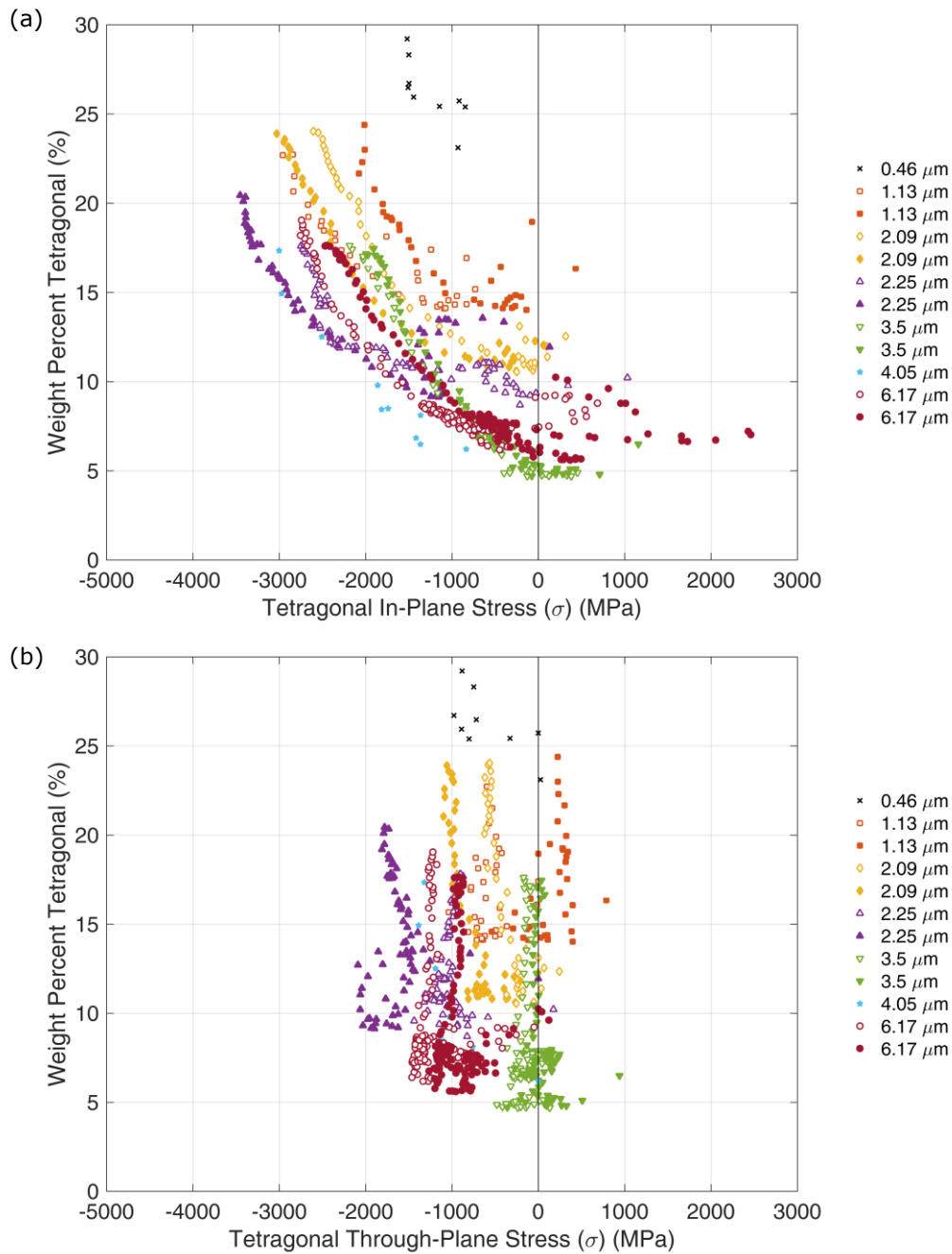
Figure 11 Plots of weight percent tetragonal oxide versus (a) tetragonal in-plane stress, and (b) tetragonal through-plane stress.

5.3. Mechanism for Transition

Early investigations into the causes of transition frequently mention the "porosity" of the oxide, sometimes in association with images of in-plane cracking [1]. Clearly, in-plane cracking does not provide the through-thickness path required to render the oxide "porous" to the environment. Rendering the oxide permeable to the environment requires a through-thickness percolation path, and a number of studies have been devoted to determining how such a path could be produced through a layer that must form in compression, investigating stresses in the oxide and the phase distribution. Correlations between averaged in-plane stresses in the monoclinic and tetragonal phases and the

22

tetragonal phase fractions have led to a number of possible explanations for the observed trends and for transition itself.

Both Zhang et al. [12] and Polatidis et al. [5] identify a relatively *sudden* decrease of the macroscopic compressive in-plane stresses at transition. They ascribe this to the stress relieving effect of lateral cracking, although this is inconsistent with the observation the lateral cracking is not a process occurring in a short time before transition: the lateral crack layer occupies approximately half the oxide thickness produced in each cycle, showing that this cracking occurs during the majority of the *time* associated with each cycle. Zhang et al. suggested that the relaxation of the compressive stress induced the cracking that gives rise to transition. However, the presence of a reduced compressive stress would not be able to produce through-plane cracking. Polatidis et al., like Yilmazbayhan et al. [2], ascribed the through-thickness path to the linkage of cracks formed during the transformation from tetragonal to monoclinic oxide. The phase change has been calculated to induce tensile stresses around the newly transformed monoclinic grains [6] and small intergranular cracks have been observed in these locations in thin transmission electron microscope foils [59].

In the present study, a *continuous* relaxation in the monoclinic in-plane stress has been observed throughout each cycle of oxidation, together with *continuous* tetragonal to monoclinic phase transformation. The proposed sequence of events leading to transition, consistent with the measured stress profiles and tetragonal phase fraction distributions, is as follows.

The rate of oxidation is initially rapid, due to direct contact between the oxidising environment and the Zircaloy metal. For further oxidation to take place, the oxidising species must diffuse through the oxide layer which is initially thin (giving a short diffusion path) and very porous (perhaps due to the dissolution of tetragonal grains in the pressurised water environment [60]), as illustrated in [16]. The initially high compressive stress in the oxide relieves via plastic deformation of the Zircaloy metal (accounting for the near-linear stress distributions in the thinner pre-transition oxides, and the introduction of high dislocation densities in the metal).

Once the oxide has reached a thickness of ~1 μm, undulations become visible (on the scale of SEM images) at the metal-oxide interface, and a further degree of stress relief occurs. The through-plane tensile stresses above delays in the oxidation front give rise to small lateral cracks, which initially hinder the diffusion of the oxidising species to the metal-oxide interface [61,62]. These appear well before transition [1,16,43]. As the oxide grows inwards, these cracks grow and open out as they experience the bulk in-plane compressive stress, whilst additional lateral cracks form at the new interface. In this way, a band of potentially interlinked lateral cracking develops in each cycle, relieving stresses closer to the metal-oxide interface.

By the time the oxide has reached 2.2-2.4 μm, the combination of plasticity in the metal and in-plane cracking finally results in stress-free (or slightly tensile in-plane stress) near the oxide surface and near the metal-oxide interface. Despite the low compressive, or even tensile, stresses, the tetragonal fraction does not disappear because of the stabilising effect of small, new oxide grains at the metal oxide interface.

At this stage, alternative explanations exist for the development of a through-thickness percolation path. The first possibility is that these macroscopic effects alone lead to through-thickness cracking, as described in '5.1. Mechanisms of Stress Relief'. When the through-plane cracks running from the oxide surface, and from the metal-oxide interface, join up with the linked band of lateral cracking, a percolation path forms between the oxide surface and the metal oxide interface. As the oxidising environment is once again able to come into contact with the underlying metal, the oxidation rate increases and transition ensues. Evidence for this percolation path was shown by Yardley et al. [63] for oxides grown on ZIRLO, via [18]O isotopic spiking of the pressurised water. The resulting [18]O profiles for the post-transition oxide showed localised penetration of the [18]O from the surface to the metal-oxide interface (via a horizontal band of higher [18]O concentration), corresponding to the vertical and lateral cracks observed via SEM.

The oxidation kinetics measured for the second cycle appear to differ slightly from the first, as seen in Figure 1. This may be due to variations in the onset of transition at different locations on the samples' surfaces. It may also be caused by direct contact occurring only at crack tips post-transition, rather than over the entire surface on initial exposure. The macroscopic lateral cracks, however, are able to act as reservoirs for the oxidising environment near the interface, limiting this effect to thin post-transition oxides.

Reports of cracking near perpendicular to the metal-oxide interface are rare in the literature. This is probably because the cracks running in from the surface are both sparsely distributed and closed by the thermal mismatch stresses induced by cooling from the autoclave temperature. On the basis of the Yardley et al. observations, only one through-thickness path need be associated with each patch of oxide going through transition. Thus, the cracks may be separated by several tens of microns. It is also noteworthy that the papers cited both used high-resolution SEMs to observe the cracks, which were very fine. The absence of observations from low-magnification investigations does not contradict the hypothesis put forward here.

A second explanation for the development of a through-thickness percolation path involves the cracking of the tensile regions around transformed tetragonal grains. The cracks could, before running into compressive regions and arresting, intensify the local tensile stresses, encouraging further transformation and cracking. If the resulting internal mosaic of cracks becomes sufficiently dense and extensive, a pathway could develop, linking the oxide surface to the band of lateral cracking.

These two proposed mechanisms are not mutually exclusive. A crack, which may have been induced by a tensile stress, is most likely to grow via the linking of small pre-existing transformation cracks/pores or, in the absence of actual transformation cracks, by the linking of the more tensile regions around transformed grains. The metal plasticity mechanism of cracking will be most significant near the outer surface, where most strain will have accumulated; near the metal-oxide interface, the oxide will have had least experience of strain in the metal, and stress relief will be dominated by the lateral cracking and transformation. Both mechanisms describe a way in which pathways are produced such that the oxidising medium can reach (or almost reach) the metal-oxide interface, leading to the accelerated corrosion (transition) observed in each subsequent cycle of oxide growth.

6. Conclusions

Nano-focus transmission XRD has been used for the first time to study the distribution with oxide depth of stresses and tetragonal:monoclinic phase fractions in Zircaloy oxides, without the need for complex deconvolution methods. In contrast to methods such as polychromatic energy-dispersive XRD, or grazing incidence XRD, which provide averages of the stresses and phase fractions that are strongly weighted toward the surface values, the use of a nano-focussed beam has enabled the stress and phase fraction distributions with depth and time to be measured directly with nano-scale resolution. It has therefore been possible to discern non-monotonic changes in the in-plane and through-plane stress distributions and tetragonal:monoclinic weight phase ratios. It has also been possible to relate these physical changes in the oxide to the oxidation rate, in particular to transition behaviour.

Detailed analyses of oxides of a range of thicknesses corresponding to the first three cycles of oxide growth has made it possible to distinguish between changes through the thickness of a given oxide film and changes at a given location over time. A full three-dimensional analysis of the stress distributions has shown that the two-dimensional approximation is only appropriate for very thin oxides (<1 μm).

The analysis has shown that both in-plane and through-plane stresses exist in the oxide for films of 1 μm and thicker. The stresses in the tetragonal oxide are not the same as those in the monoclinic oxide. Both the in-plane and through-plane stresses are more compressive in the tetragonal phase.

Previous observations of the continuous production of dislocations at the metal-oxide interface have been linked to the stress measurements. It is proposed that, as the oxide moves into the metal, incremental plastic strains in newly stressed layers of metal lead to accumulated strains in the oxide. This process relieves the compressive stress in the oxide, producing a trend of increasing stress reduction with increasing age of the oxide i.e. reducing compression with reducing distance from the oxide surface. Ultimately, it leads to tensile in-plane stresses in the oxide at the surface that are relieved by cracking. Further increments of plasticity in the metal extend these cracks, probably via the linkage of pores or microcracks present as a result of phase transformations.

In the latter halves of each cycle, additional stress relief results from the growth of undulations at the metal-oxide interface, and the formation and opening out of lateral cracks. This additional stress relief is also continuous.

The tetragonal oxide content is highest at the metal oxide interface when the compressive stresses are highest and the grain size small. Grain growth and stress relief progressively reduce the tetragonal phase fraction at any location as the interface moves into the metal. The transformation of the tetragonal grains to monoclinic may also induce local stresses, possibly producing a mosaic of transformation cracks as the prevailing background stress reduces.

Previous authors have deduced or observed that transition ensues when a through-thickness percolation path allows the environment to reach the metal-oxide interface. This study has revealed that a stress relief process in the metal substrate imposes expansion on the oxide in such a way as first to relieve oxide compressive stress and then to promote through-thickness cracking. The development of the percolation path need not rely only on the stress changes induced by plasticity in the metal substrate. It can incorporate linked in-plane cracks nucleated at delays in the oxidation front as well as microcracks induced by earlier transformations of tetragonal grains.

Acknowledgements

References

[1] B. Cox, Journal of Nuclear Materials, 336, 2005, 331.

[2] A. Yilmazbayhan, A. T. Motta, R. J. Comstock, G. P. Sabol, B. Lai, Z. Cai, Journal of Nuclear Materials, 324, 2004, 6-22.

[3] N. Petigny, P. Barberis, C. Lemaignan, Ch. Valot, M. Lallemant, Journal of Nuclear Materials, 280, 2000, 318-330.

[4] B. Cox, V. G. Kritsky, C. Lemaignan, V. Polley, I. G. Ritchie, H. Ruhmann, V. N. Shishov, Yu. K. Bibilashvili, A. V. Nikulina, "Waterside Corrosion of Zirconium Alloys in Nuclear Power Plants", IAEA TECDOC-996, publ. IAEA, Vienna, 1998.

[5] E. Polatidis, P. Frankel, J. Wei, M. Klaus, R. J. Comstock, A. Ambard, S. Lyon, R. A. Cottis, M. Preuss, Journal of Nuclear Materials, 432, 2013 102.

[6] P. Platt, P. Frankel, M. Gass, R. Howells, M. Preuss, "Phase Transformations & Degradation in Zirconium Oxide Layers", Poster Presentation at 'Zirconium in the Nuclear Industry, 17th International Symposium', Hyderabad, India, 2013.

[7] H. Arashi and J. M. Ishigame, Physica Status Solidi (a), 71, 2, 1982, 313-321.

[8] J. Godlewski, J. P. Gros, M. Lambertin, J. F. Wadier and H. Weidlinger, in Zirconium In The Nuclear Industry: 9th Int. Symp, ASTM STP 1132, Eds. C. M. Eucken and A. M. Garde, pub. ASTM, Philadelphia, USA, 1991, 416-436.

[9] R. C. Garvie and M. F. Goss, Journal of Materials Science, 21, 1986, 1253-1257.

[10] R. C. Garvie, Journal of Physical Chemistry, 82, 1978, 218-224.

[11] S. Shulka and S. Seal, International Materials Review, 50, 2005, 1-20.

[12] H. X. Zhang, D. Fruchart, E. K. Hlil, L. Ortega, Z. K. Li, J. J. Zhang, J. Sun, L. Zhou, Journal of Nuclear Materials, 396, 2010, 65-70.

[13] P. Platt, E. Polatidis, P. Frankel, M. Klaus, M. Gass, R. Howells, M. Preuss, Journal of Nuclear Materials, 456, 2015, 415-425.

[14] N. Petigny, P. Barberis, C. Lemaignan, Ch. Valot, M. Lallemant, Journal of Nuclear Materials, 280, 2000, 318-330.

[15] M. Preuss, P. Frankel, S. Lozano-Perez, D. Hudson, E. Polatidis, N. Ni, J. Wei, C. English, S. Storer, K. B. Chong, M. Fitzpatrick, P. Wang, J. Smith, C. Grovenor, G. Smith, J. Sykes, B. Cottis, S. Lyon, L. Hallstadius, R. J. Comstock, A. Ambard, M. Blat-Yrieix, 16th International Symposium on Zirconium in the Nuclear Industry, ASTM STP1529, 8, 9, 2011, 649.

[16] S. Ortner, H. Swan, A. Laferrere, C. English, J. Hyde, P. Styman, K. Jurkschat, H. Hulme, A. Pantelli, M. Gass, V. Allen, P. Frankel, Fontevraud 8 – Contribution of Materials Investigations and Operating Experience to LWRs' Safety, Performance and Reliability, France, Avignon, 2014.

[17] H. Swan, S. Ortner, J. Hyde, and C. English, H. Hulme, M. Gass, V. Allen, Poster Presentation, 17th International Symposium on Zirconium in the Nuclear Industry, 2013.

[18] J. Lin, H. Li, J. A. Szpunar, R. Bordoni, A. M. Olmedo, M. Villegas, A. J. G. Maroto, Materaterials Science and Engineering, 381, 2004, 104.

[19] N. Ni, S. Lozano-Perez, M. L. Jenkins, C. English, G. D. W. Smith, J. M. Sykes, C. R. M. Grovenor, Scripta Materialia, 62, 2010, 564.

[20] A. Garner, A. Gholinia, P. Frankel, M. Gass, I. MacLaren, M. Preuss, Acta Materialia 80, 2014, 159–171.

[21] F. Garzarolli, H. Seidel, R. Tricot, J. Gros, Zirconium In the Nuclear Industry: Ninth International Symposium, ASTM STP 1132, 1991.

[22] D. Pêcheur, J. Godlewski, J. Peybernes, L. Fayette, M. Noé, A. Frichet and O. Kerrec, in 12th International Symposium on Zirconium in the Nuclear Industry, ASTM STP 1354, Eds. G. P. Sabol and G. D. Moan, pub. ASTM, West Conshohocken, USA, 2000, 793-811.

[23] A. Nechaev, "Corrosion of zirconium alloys in nuclear power plants", IAEA TECDOC-684, publ. IAEA, Vienna, 1993.

[24] G. Vaughan et al., in Proceedings of the 31st Risoe International Symposium on Materials Science, 2010.

[25] A. P. Hammersley, *ESRF Internal Report*, ESRF97HA02T, 1997.

[26] A. P. Hammersley, S. O. Svensson, and A. Thompson, Nuclear Instruments and Methods in Physics Research Section A: Accelerators, Spectrometers, Detectors and Associated Equipment, A346, 1994 312-321.

[27] A. P. Hammersley, S. O. Svensson, M. Hanfland, A. N. Fitch, D. Häusermann, High Pressure Research, 14, 1994, 235-248 .

[28] H. Rietveld, Journal of Applied Crystallography, 2, 1969, 65-71.

[29] P. Thompson, D.E. Cox, J.B. Hastings, Journal of Applied Crystallography, 20, 1987, 79.

[30] B. H. O'Connor, S. Pratapa, Advances in X-ray Analysis, 45, 2002, 158-165.

[31] *Standard and Reference Materials for Environmental Science*, NOAA Technical Memorandum NOS ORCA 94, 1995.

[32] R. W. G. Wyckoff, Crystal Structures, 1, 1963, 239-444.

[33] D. Kaiser, R. Watters, "Certificate of Analysis - Standard Reference Material 674b", National Institute of Standards & Technology, 2012, 1-5.

[34] R. J. Hill, L.M.D. Cranswick, Journal of Applied Crystallography, 27, 1994, 802-844

[35] R. W. G. Wyckoff, Crystal Structures, 1, 1963, 7-83.

[36] G. Teufer, Acta Crystallographica, 15, 1962, 1187.

[37] S. C. Nh, B. N. Brockhouse, E. D. Hallman, Materials Research Bulletin, 2, 1967, 69.

[38] L. H. Beck, C. S. Smith, Transactions of the American Institute of Mining, Metallurgical and Petroleum Engineers, 194, 1952, 1079.

[39] W. P. Davey, Physical Review, 25, 1925, 753-761.

[40] B. D. Cullity, "Elements of X-ray Diffraction", Addison-Wesley Publishing Company Inc., 1967, 436.

[41] P. S. Prevéy, "X-ray Diffraction Residual Stress Techniques," Metals Handbook, 10, Metals Park: American Society for Metals, 1986, 380-392.

[42] P. J. Withers, M. Preuss, A. Steuwer, J. W. L. Pang, Journal of Applied Crystallography, 40, 2007, 891.

[43] P. Bossis, G. Lelièvre, P. Barberis, X. Iltis and F. Lefebvre, in Zirconium In The Nuclear Industry: 12th International Symposium, ASTM STP 1354, Eds. G. P. Sabol and G. D. Moan, pub. ASTM, West Conshohocken, USA, 2000, 918-945.

[44] A. T. Motta, A. Yilmazbayhan, R. J. Comstock, J. Partezana, G. P. Sabol, B. Lai and Z. Cai, in Zirconium In The Nuclear Industry: 14th Int. Symp, ASTM STP 1467, Eds. P. Rudling and B. Kammenzind, pub. ASTM, West Conshohocken, USA, 2005 205-232.

[45] P. Tejland and H.-O. Andrén, Journal of Nuclear Materials, 444, 2014, 30-34.

[46] N. Petigny, P. Barberis, C. Lemaignan, Ch. Valot, M. Lallemant, Journal of Nuclear Materials, 280, 2000, 318-330.

[47] M. Parise, O. Sicardy and G. Cailletaud, Journal of Nuclear Materials, 256, 1998, 35-46.

[48] N. Ni, D. Hudson, J. Wei, S. Lozano-Perez, G. D. W. Smith, J. M. Sykes, S. S. Yardley, K. L. Moore, S. Lyon, R. Cottis, M. Preuss and C. R. M. Grovenor, Acta Materialia, 60, 2010, 7132-7149.

[49] P. Platt, P, Frankel, M. Gass, R. Howells, M. Preuss, 'Phase Transformations and Degradation in Zirconium Oxide Layers, Poster Presentation, 17th ASTM Symposium on Zirconium in the Nuclear Industry, 2013.

[50] J. Wei, P. Frankel, E. Polatidis, M. Blat, A. Ambard, R. J. Comstock, L. Hallstadius, D. Hudson, G. D. W. Smith, C. R. M. Grovenor, M. Klaus, R. A. Cottis, S. Lyon and M. Preuss, Acta Materialia, 61, 11, 2013, 4200-4214.

[51] J. Lin, H. Li, C. Nam, J. A. Szpunar, Journal of Nuclear Materials, 334, 2004, 200.

[52] D. J. Spengler, A. T. Motta, R. Bajaj, J. R. Seidensticker, Z. Cai, Journal of Nuclear Materials., 464, 2015, 107-118.

[53] S. Block, J. A. H. Da Jornada and G. J. Piermarini, Journal of the American Ceramics Society, 68, 9, 1985, 497-499.

[54] H. Arashi, J. M. Ishigame, Physica Status Solidi 71, 2, 1982, 313.

[55] P. Barberis, Journal of Nuclear Materials, 226, 1-2, 1995, 34-43.

[56] B. De Gelas, G. Beranger and P. Lacombe, Journal of Nuclear Materials, 28, 1968 185-194.

[57] B. Cox and H. I. Sheikh, Journal of Nuclear Materials, 249, 1997, 17-32.

[58] K. Takeda and H. Anada, in *Zirconium In The Nuclear Industry: 12th Int. Symp, ASTM STP 1354*, Eds. G. P. Sabol and G. D. Moan, pub. ASTM, West Conshohocken, USA, 2000, 592-608.

[59] P. Bossis, J. Thomazet and F. Lefebvre, in Zirconium In The Nuclear Industry: 13th Int. Symp, ASTM STP 1423, Eds. G. D. Moan and P. Rudling, pub. ASTM, West Conshohocken, USA, 2002, 190-221.

[60] M. Oskarsson, E. Ahlberg and K. Pettersson, Journal of Nuclear Materials, 295, 2001, 126-130.

[61] M. Tupin, F. Valdivieso, M. Pijolat, M. Soustelle, A. Frichet, P. Barbéris, Materials Science Forum, 461-464, 2004, 13-20.

[62] M. Tupin, M. Pijolat, F. Valdivieso, M. Soustelle, A. Frichet and P. Barberis, , Journal of Nuclear Materials, 317, 2003 130-144.

[63] S. S. Yardley, K. L. Moore, N. Ni, J. F. Wei, S. Lyon, M. Preuss, S. Lozano-Perez and C. R. M. Grovenor, Journal of Nuclear Materials, 443, 2013, 436-443.